JOURNAL OF GEOPHYSICAL RESEARCH, VOL. 117, D02109, doi:10.1029/2011JD016321, 2012

Testing convective transport on short time scales: Comparisons with mass divergence and ozone anomaly patterns about high rain events

Toni Mitovski,[1] Ian Folkins,[1] Randall V. Martin,[1,2] and Matthew Cooper[1]

Received 29 May 2011; revised 21 November 2011; accepted 22 November 2011; published 26 January 2012.

[1] High rain events in the western tropical Pacific were identified using the Tropical Rainfall Measuring Mission (TRMM) 3B42 gridded rainfall data set. Horizontal wind measurements from radiosonde arrays, cloud top frequency measurements from CALIPSO, and ozonesonde measurements from SHADOZ were used to construct anomaly patterns of divergence, cloud top frequency, and ozone mixing ratio about the high rain events. The observed divergence anomaly pattern was compared with patterns produced by the Goddard Earth Observing System version 4 (GEOS-4) and GEOS-5 assimilated meteorological data sets. The midlevel (~6 km) divergence dipole seen in observations, consisting of a local maximum in divergence 8 h before peak rainfall and a local maximum in convergence 8 h after peak rainfall, is not represented in the GEOS-4 or GEOS-5 meteorology. The ozone anomaly pattern shows ozone decreases at midlevels (3–8 km) up to 16 h prior to peak rainfall. These decreases occur in association with increases in the frequency of midlevel cloud tops and are due to increased detrainment from cumulus congestus clouds. The observed ozone anomaly pattern was compared with anomaly patterns produced by the GEOS-Chem chemical transport model, driven by GEOS-4 and GEOS-5 assimilated winds and temperatures. The GEOS-Chem simulations also exhibit negative ozone anomalies at midlevels in association with high rain events. However, these anomalies are nearly symmetric about peak rainfall, rather than strongest prior to peak rainfall. The upper level negative ozone anomalies of the models are more persistent than the observations. These results help characterize some of the difficulties of meteorological data sets in capturing the layered character of tropical convective outflow and its timing with respect to high rain events.

Citation: Mitovski, T., I. Folkins, R. V. Martin, and M. Cooper (2012), Testing convective transport on short time scales: Comparisons with mass divergence and ozone anomaly patterns about high rain events, *J. Geophys. Res.*, *117*, D02109, doi:10.1029/2011JD016321.

1. Introduction

[2] Short-lived species can be transported within convective clouds from the boundary layer to the free troposphere and affect the local rates of ozone and aerosol production. The accuracy of convective transport in global models is often tested using monthly or seasonal distributions of relative humidity and other chemical tracers [*Bey et al.*, 2001; *Folkins et al.*, 2006]. However, it is possible in principle for a model to generate realistic distributions of chemical tracers on monthly time scales, even if the short time scale convective events which give rise to this distribution are not accurately represented.

[3] Assessing the accuracy of convective transport in a global model is a challenge. It is difficult to directly compare in situ measurements of chemical tracers from aircraft with models because models rarely simulate the details of a particular convective event with sufficient accuracy to make point-by-point comparisons meaningful. However, tropical convection often exhibits a repetitive sequence of vertical motions, the so-called building block pattern [*Mapes et al.*, 2006], in which midlevel congestus clouds are followed by deep cumulonimbus clouds, which are then followed by precipitating stratiform anvil clouds. The existence of this pattern suggests that it may be useful to construct anomaly patterns of chemical tracers in the time-height plane about high rain events using a long time series of observed profiles above a fixed location, and compare the results with models. The main practical difficulty with this approach is that it requires at least several hundred vertical profiles of a chemical tracer to develop statistically robust anomaly patterns.

[4] Here we use a 12 year record of ozonesondes (1998–2009) at Fiji and Samoa from the Southern Hemisphere

---

[1] Department of Physics and Atmospheric Science, Dalhousie University, Halifax, Nova Scotia, Canada.

[2] Harvard-Smithsonian Center for Astrophysics, Cambridge, Massachusetts, USA.

0148-0227/12/2011JD016321

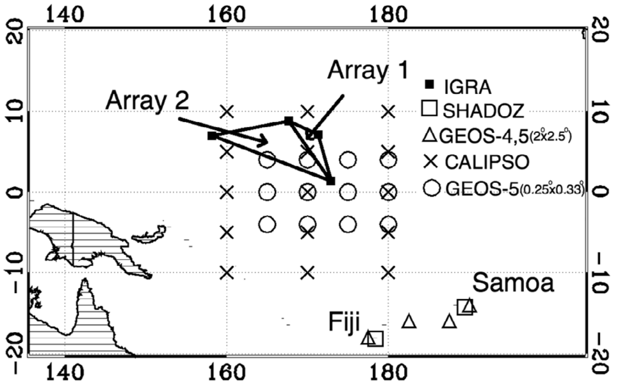

Figure 1. A map showing the locations of various observations used in this paper. Radiosonde (Integrated Global Radiosonde Archive, IGRA) locations are represented with solid squares. The two SHADOZ sites (Fiji and Samoa) are indicated with open squares. The open triangles show the GEOS-Chem (GEOS-4, GEOS-5) grid locations used to define the divergence and ozone anomaly patterns of the models. The open circles show the GEOS-5 YOTC grid locations. The CALIPSO locations are indicated by crosses.

Additional Ozonesondes (SHADOZ) campaign [*Thompson et al.*, 2003] to construct ozone anomaly patterns about high rain events. The rain events at Fiji and Samoa were identified using the Tropical Rainfall Measuring Mission (TRMM) 3B42 gridded rainfall product [*Kummerow et al.*, 1998]. The growth and decay of the rain events we selected typically occurred over a 10–20 h period. When constructing the ozone anomaly patterns, we therefore looked for ozonesondes that occurred within 24 h of a rain event.

[5] The imprint produced by a convective cloud on the background distribution of a chemical tracer will be strongly influenced by how the cloud mixes with its environment, and in particular, its vertical profiles of convective entrainment and detrainment. Within an area containing a group of convective clouds, the sum of mass entrainment and detrainment is approximately equal to the mass divergence. Divergence anomaly patterns about high rain events are therefore useful for interpreting tracer anomaly patterns. Calculations of mass divergence require at least a triangular array of horizontal wind measurements. Because of the absence of nearby radiosonde stations, it was not possible to calculate mass divergence profiles at Fiji or Samoa. Mass divergence anomaly patterns about high rain events were therefore constructed using measurements from two nearby radiosonde arrays.

[6] The outflow from deep convection gives rise to pronounced features in the climatological profiles of mass divergence, ozone [*Pickering et al.*, 1993, 2001; *Kley et al.*, 1996; *Folkins et al.*, 2002, 2006; *Solomon et al.*, 2005; *Avery et al.*, 2010], and other chemical tracers [*Lelieveld and Crutzen*, 1994; *Lawrence et al.*, 1999, 2003; *Nassar et al.*, 2009; *Liu et al.*, 2010]. Detrainment from congestus clouds gives rise to a second layer of preferred convective outflow near the melting level (~5.5 km). The existence of the congestus outflow layer is supported by measurements of cloud top height [*Zuidema*, 1998; *Dessler et al.*, 2006], mass divergence [*Thompson et al.*, 1979; *Mapes et al.*, 2006; *Mitovski et al.*, 2010], and relative humidity [*Johnson et al.*, 1999]. In this paper, we use ozone measurements to demonstrate the existence of the congestus outflow layer.

[7] Unlike the deep outflow layer, the congestus outflow layer does not give rise to a local maximum in climatological profiles of mass divergence, or to a local minimum in climatological profiles of ozone mixing ratio. Anomaly patterns about high rain events are therefore essential for demonstrating the existence of the congestus mode, and for assessing its impact on the mass and ozone budgets of the tropical atmosphere.

[8] The outline of the paper is as follows. In section 2 we give background information on the various data sets used in the paper. In section 3, we first give a meteorological overview of the rain events at Fiji and Samoa. We then discuss the methodology used to define the divergence anomaly patterns of two nearby radiosonde arrays. The observed divergence anomaly patterns are compared with patterns produced from the GEOS-4 and GEOS-5 assimilated meteorological data sets. We conclude section 3 with a discussion of the cloud top frequency anomaly patterns about high rain events obtained from the CALIPSO instrument. The focus of section 4 is the construction of an ozone anomaly pattern about high rain events using the SHADOZ data set, and its comparison with output from the GEOS-Chem chemical transport model. In section 5, we argue that the observed ozone anomaly patterns are not strongly influenced by lightning generated NO. The main arguments of the paper are summarized in section 6.

2. Description of Data Sets

2.1. TRMM 3B42 Rainfall

[9] We used the TRMM 3B42 gridded rainfall product to identify rain events at various tropical locations. The TRMM rainfall estimates are constructed from combining several satellite borne instruments, including a precipitation radar, a multichannel microwave radiometer, and visible and infrared sensors [*Kummerow et al.*, 1998]. The data set has a resolution of 3 h (centered at the standard synoptic times of 00:00, 03:00, 06:00, 09:00, 12:00, 15:00, 18:00, and 21:00 UTC), a horizontal resolution of 0.25° × 0.25°, and extends from 1998 to the present.

2.2. SHADOZ Ozone

[10] SHADOZ is an archive of ozonesonde profiles from 13 tropical locations [*Thompson et al.*, 2003]. The soundings have been launched approximately two times per month since 1998, and provide high-resolution profiles of ozone mixing ratio. For this analysis, it was desirable to use data from ozonesonde stations located within oceanic regions characterized by frequent deep convection. The presence of a strong diurnal cycle in the timing of the rain events would have hindered our analysis. We were therefore restricted to islands sufficiently small that the timing of the rain events was not strongly affected by the local sea breeze circulation. The most useful stations were Fiji (18.13°S, 178.40°E) and Samoa (14.23°S, 170.56°W). Between 1998 and 2009, there were 275 ozonesonde launches at Fiji, and 416 launches at Samoa. The locations of Fiji and Samoa are denoted in Figure 1 by open squares.

2.3. Integrated Global Radiosonde Archive Horizontal Wind

[11] The Integrated Global Radiosonde Archive (IGRA) data set contains radiosonde profiles stored at the National

Climatic Data Center [*Durre et al.*, 2006]. Horizontal wind measurements from these radiosondes, available at 00:00 and 12:00 UTC, are stored on the standard pressure levels of 1000, 925, 850, 700, 500, 400, 300, 250, 200, 150, and 100 hPa. We used horizontal wind data to calculate the mass divergence profiles of two adjacent triangular arrays, denoted array 1 and array 2. The locations of these two triangular arrays are shown in Figure 1. Most of the IGRA radiosonde locations have records for the past 30–40 years. Because of the availability of TRMM rainfall data, we used IGRA wind data from 1998 to 2009. Array 1 used radiosonde measurements from Kwajalein Atoll (8.73°N, 167.73°E), Majuro Atoll (7.08°N, 171.38°E), and Tarawa (1.35°N, 172.92°E). It has an area of 112,000 km^2, roughly corresponding to the area of a 3° × 3° grid box at the equator. Array 2 also used wind data from Kwajalein Atoll and Tarawa, with the third radiosonde location being Ponape (6.97°N, 158.22°E). It has an area of roughly 480,000 km^2, about four times larger than array 1.

2.4. CALIPSO Cloud Tops

[12] We used cloud top information from the Cloud-Aerosol Lidar and Infrared Pathfinder Satellite Observation (CALIPSO) level 2 cloud layer product [*Winker et al.*, 2009]. The data are available in a variety of horizontal resolutions. The 1 km horizontal resolution profiles used here are produced from three profiles, each with a horizontal resolution of 0.33 km and a vertical resolution of 30 to 60 m in the troposphere. The detection of cloud tops is based in part on the existence of strong vertical gradients in the backscattered intensity, and an individual profile may be associated with multiple cloud tops. The likelihood of detecting a cloud top at lower altitudes is reduced when obscured by thick clouds at higher altitude. Here, we examined all CALIPSO profiles within the 15 2° × 2° grid cells between 10°N and 10°S, and between 160°E and 180°E. These grid cells are represented by crosses in Figure 1. This oceanic region is close to Fiji and Samoa, and is characterized by frequent deep convection. There were 648,730 one kilometer horizontal resolution CALIPSO profiles available within the 15 2° × 2° grid cells used here between June 2006 and December 2009.

[13] The CALIPSO instrument is on a satellite with a Sun-synchronous polar orbit that crosses the equator twice a day. There is a modest variation in the local crossing time over the 15 grid cells during the course of a year. The first crossing occurs between 01:08 and 03:00 UTC, while the second crossing occurs between 13:27 and 15:06 UTC. Local solar noon has an annual variation of 23:50 to 01:35 UTC over the 15 grid cells. The first crossing time therefore tends to occur about an hour after solar noon while the second crossing occurs about an hour after local midnight.

2.5. GEOS-4 and GEOS-5 Assimilated Meteorology

[14] Mass divergence anomaly patterns about high rain events were calculated in three assimilated meteorological data sets. The GEOS-4 and GEOS-5 data sets are produced by the Goddard Earth Observing System (GEOS) at the NASA Global Modeling and Assimilation Office (GMAO). We used GEOS-4 and GEOS-5 data from January 2004 to December 2006. Both are archived at a horizontal resolution of 2° × 2.5°. GEOS-4 has 19 vertical layers in the troposphere, while GEOS-5 has 36 vertical layers. The GEOS-4 and GEOS-5 data sets used here were also used to drive the GEOS-Chem model, and have a temporal resolution of 3 h for rainfall, and 6 h for the 3-D variables.

[15] GEOS-4 and GEOS-5 have different treatments of moist convection. GEOS-4 employs the Zhang and McFarlane parameterization [*Zhang and McFarlane*, 1995] for deep convection, and the Hack scheme [*Hack*, 1994] for shallow convection. GEOS-5 employs the relaxed Arakawa-Schubert convective parameterization for shallow and deep moist convection [*Moorthi and Suarez*, 1992].

[16] We also used a higher spatial resolution 0.25° × 0.33° version of GEOS-5, made available from January 2009 to December 2009 as part of Year of Tropical Convection (YOTC). This data set was archived at a temporal resolution of 1 h for rainfall, and 3 h for 3-D variables.

2.6. The GEOS-Chem Chemical Transport Model

[17] The GEOS-Chem chemical transport model [*Bey et al.*, 2001] version v8-03-01 (http://www.geos-chem.org) can be driven by a variety of meteorological data sets. The GEOS-Chem simulations discussed here were driven by the GEOS-4 and GEOS-5 assimilated meteorological data sets described above. These simulations extend from January 2004 to December 2006.

3. Meteorological Background

3.1. Rain Event Definition

[18] The ozone anomaly pattern produced by a group of rain events will be sensitive to the spatial extent, duration, and intensity of the events. We first averaged the 0.25° × 0.25° TRMM 3B42 rainfall data set to a lower spatial resolution of 2° × 2°. This ensured that the size of the observed rain events would be similar to the GEOS-4 and GEOS-5 grid resolution.

[19] Rain events were considered to occur at Fiji or Samoa if the 3 h rain rate at the 2° × 2° TRMM grid cell containing one of these islands exceeded a particular threshold. The selection of this threshold requires a compromise between the number of rain events and their intensity. We wanted the rain event threshold to be large enough that the rain events would be associated with significant perturbations in the ozone mixing ratio from climatology. On the other hand, given the limited number of ozonesondes at Fiji and Samoa, the rainfall event threshold had to be small enough that a sufficient number of ozonesonde profiles would be available to construct the ozone anomaly patterns. By using a rain event threshold of 1.5 mm/h, there were 116 ozonesondes at Samoa and 158 ozonesondes at Fiji, between 1998 and 2009, that occurred within 24 h of a 2° × 2° 3 h TRMM rain event. Rain events of this intensity were sufficiently infrequent at the other oceanic SHADOZ locations that the use of ozonesondes from these additional locations would not have contributed significantly to the number of ozonesondes available.

[20] Figure 2 shows the spatial variation of the average rainfall anomaly at Fiji and Samoa for all rain events at these two locations using the above definition. The maps were obtained by first determining the rainfall distribution at Fiji and Samoa during a rain event using the native 0.25° × 0.25° resolution. After subtracting the appropriate seasonal mean from each high-resolution rainfall map, the high

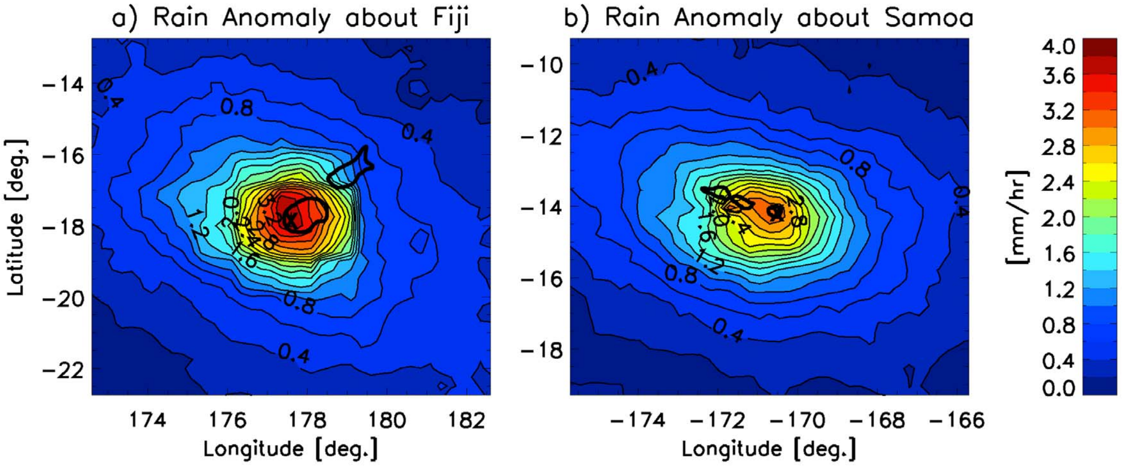

Figure 2. The rain anomaly map about high rain events for (a) Fiji and (b) Samoa. The locations of the sounding sites are at the center of each plot and are represented with crosses. The outlines of the islands are indicated with thick black lines. The rain anomaly map is an average of the rain anomaly maps for all rain events during the 1998–2009 period. In calculating the rain anomaly about a rain event, we used the 0.25° 3B42 TRMM gridded rainfall data set.

spatial resolution rainfall anomalies from all rain events at each location were added together. The 2° × 2° TRMM rain events at Fiji and Samoa are clearly larger than their respective islands, spread significantly outside the 2° × 2° boxes used in their definition, and synoptic in scale (rather than being associated with mesoscale diurnal circulations).

[21] The locations of the ozonesonde stations at Fiji and Samoa are denoted by crosses in Figure 2. Within a rain event, the effect of convection on the ambient ozone mixing ratio can be expected to scale with the convective mass fluxes, which should scale with the rain rate. The ozone anomalies associated with the rain events should therefore also be synoptic in scale, rather than being localized to the ozonesonde stations. The relative influence of horizontal advection on the ambient ozone mixing ratio can be expected to be larger on the periphery of an event.

[22] The rain events at Fiji and Samoa are typically quite short. Figure 3a shows the composite rain event profile obtained by averaging over all rain events at Fiji and Samoa that were associated with at least one ozonesonde. The time at which the rain event is defined corresponds to t = 0 on the horizontal axis. During a rain event, the rain rate decreases to one half of peak intensity within about 4 h of peak rainfall. Two vertical lines in Figure 3a indicate this time interval. There is also some enhancement in rain rate above background for up to 20 h prior to peak rainfall.

[23] The GEOS-4 and GEOS-5 rain events were defined using a procedure similar to that used for the TRMM rain events. However, the frequency of occurrence of high rainfall rates in the GEOS-4 and GEOS-5 rainfall data sets is substantially less than in the TRMM 2° × 2° rainfall data set. Figure 3b shows that the frequency of occurrence of rainfall rates in excess of 1.5 mm/h is very low. In order to obtain a reasonable number of GEOS-4 and GEOS-5 rain events, we therefore adopted a reduced rain event threshold of 1.0 mm/h. Two vertical lines in Figure 3b show the 1.0 and 1.5 mm/h rain thresholds.

[24] We further increased the number of GEOS-4 and GEOS-5 rain events by considering rain events not only at the two grid points containing Fiji (18°S, 177.5°E) and Samoa (14°S, 170°W), but also at the two nearby grid cells of (16°S, 177.5°W) and (16°S, 172.5°W). The four grid cells used to define the GEOS-4 and GEOS-5 rain events are indicated by open triangles in Figure 1.

3.2. Diurnal Issues

[25] Figure 4a shows the diurnal variation of the mean TRMM rain rate in the 2° × 2° grid cells containing Fiji and Samoa between 1998 and 2009. Local solar noon varies between 23:50 and 00:20 UTC over the course of a year at Fiji, and between 23:10 and 23:40 UTC at Samoa. Over land, the diurnal cycle in tropical rainfall tends to exhibit a peak in the late afternoon or early evening [*Nesbitt and Zipser*, 2003]. Over the oceans, the amplitude of the diurnal cycle is much smaller, with a tendency for peak rainfall early in the morning [*Nesbitt and Zipser*, 2003]. Figure 2 shows that the land area of the Fijian and Samoan islands is smaller than the TRMM 2° × 2° grid cells within which they are located. The diurnal cycle in rainfall within the two grid cells is therefore likely to be affected by both land and ocean forcings. Figure 4a shows there is a weak diurnal cycle at both grid cells. The diurnal cycle at the Samoan grid cell (solid curve) exhibits an early morning peak and appears to be more strongly influenced by the ocean. The diurnal cycle at the Fijian grid cell (dashed curve) exhibits an afternoon peak and appears to be more strongly influenced by land.

[26] Figure 4b shows the diurnal variation in the total number of TRMM rain events at the two grid cells containing Fiji and Samoa, plotted as the number of rain events per 3 h interval between 1998 and 2009, using the rain event definition discussed above. There is a tendency for the rain events of the Samoan grid cell to occur near sunrise (about 12:00 UTC). A particular rain event contributes to the ozone anomaly pattern at Fiji or Samoa only if there is an

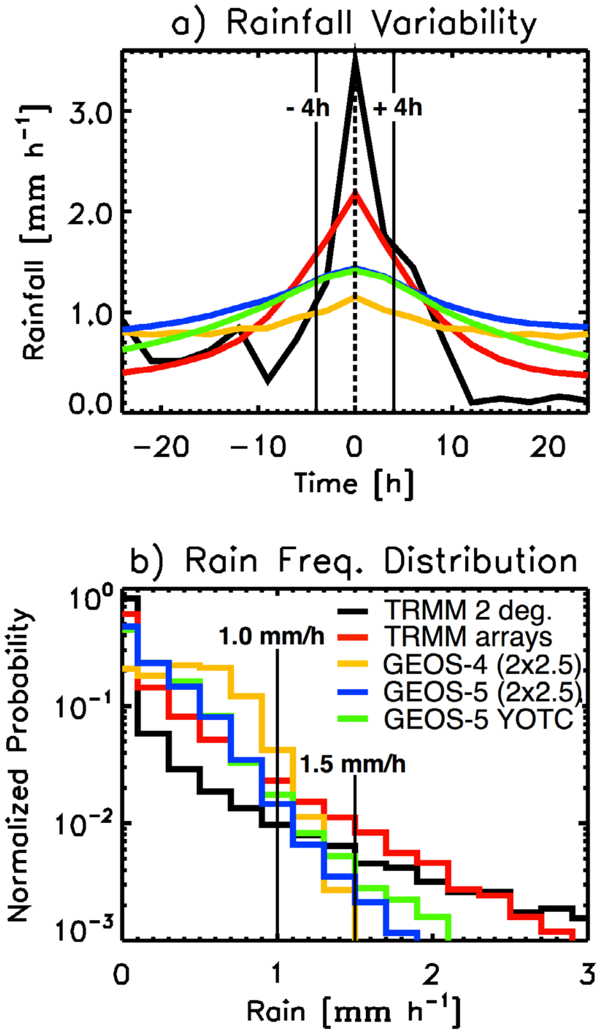

Figure 3. (a) Variation in time of the mean rainfall rate during the rain events associated with various rainfall data sets; t = 0 corresponds to the time at which the rain event is defined. (b) Rain frequency distribution per 0.2 mm/hr rainfall bin. The black line shows TRMM 3B42 2° × 2° rain frequency distribution, the red line shows TRMM 3B42 over arrays, the gold line shows GEOS-4 2° × 2.5°, the blue line shows GEOS-5 2° × 2.5°, and the green line shows GEOS-5 0.25° × 0.33° rain frequency distribution.

ozonesonde launched within 24 h of the event. Figure 4d shows that the ozonesondes at Fiji and Samoa tend to be launched near local solar noon. The diurnal cycle in the timing of the subset of the rain events used to produce the ozone anomaly patterns is shown in Figure 4c. At both Fiji and Samoa, the diurnal cycle in the number of rain events that occur within 24 h of an ozonesonde launch is weak.

3.3. Mass Divergence Anomaly Patterns From Observations

[27] Convective clouds affect the concentrations of chemical tracers in the background atmosphere partly by entraining air from their environment and by detraining air into their environment. Within a population of growing convective clouds, entrainment usually exceeds detrainment at low levels, giving rise to a net horizontal transport of mass from the background atmosphere toward the growing clouds. This inward horizontal transport is ordinarily associated with low-level convergence. Conversely, the atmosphere tends to be divergent at height regions where detrainment exceeds entrainment. Preferred layers of inflow and outflow can be diagnosed from mass divergence anomaly patterns. These divergence patterns help interpret the anomaly patterns obtained from chemical tracers such as ozone.

[28] Mass divergence anomaly patterns can be calculated using simultaneous horizontal winds from triangular arrays of radiosondes, launched either as part of an intensive field campaign [e.g., *Mapes et al.*, 2006], or from routine radiosonde profiles over land [*Mitovski et al.*, 2010]. Here, we use routine horizontal wind observations over a 12 year period (1998–2009) from two radiosonde arrays in the IGRA archive (called array 1 and array 2) near Kwajalein to diagnose the vertical variation of the net convective inflow and outflow associated with rain events over the western tropical Pacific Ocean. The locations of the two arrays are shown in Figure 1. Arrays 1 and 2 were chosen in part because they are close to Fiji and Samoa. The divergence anomaly patterns of the two arrays should therefore be similar to the divergence patterns of the rain events at Fiji and Samoa. In addition, because both arrays have an area comparable with a 2° × 2° grid cell, their divergence anomaly patterns can be compared with those calculated from the GEOS-4 and GEOS-5 assimilated meteorological data sets.

[29] Individual divergence profiles were first constructed from IGRA horizontal wind observations by interpolation from the vertices of each radiosonde array to the center of each side. The seasonal mean divergence profiles of the two standard radiosonde launch times were constructed for each array by averaging over the individual profiles.

[30] Rain events at arrays 1 and 2 were determined by first calculating a time series of the average rain rate within each array from the high resolution 0.25° × 0.25° TRMM rainfall product. Figure 3b shows the frequency distribution of the TRMM rain rate averaged over each of the two arrays. It is similar to the frequency distributions associated with the 2° × 2° Samoan and Fijian grid cells. Rain events within the two arrays were therefore considered to also occur at times when the average rain rate within each array exceeded a 1.5 mm/h threshold. With this choice, there were 1339 mass divergence profiles at array 1, and 805 divergence profiles at array 2, that occurred within 24 h of a rain event. Mass divergence anomalies were calculated by subtracting from the individual profiles the seasonal mean divergence profile with the same launch time. The divergence anomaly profiles were then grouped into 3 h time bins on the basis of the time difference between the time of the divergence measurement and the time of the rain event. The anomaly profiles were then averaged to produce a composite mass divergence anomaly pattern for each array. These are shown in Figure 5a and 5b.

[31] The mass divergence anomaly patterns of arrays 1 and 2 are similar. Both exhibit convergence near the surface prior to peak rainfall, a strong upper level divergence near 13 km at t = 0, and an antisymmetric divergence dipole near 6 km. The strong upper level divergence centered at peak rainfall is presumably due to deep convection. The midlevel divergence dipole consists of a divergence 8 h prior to peak

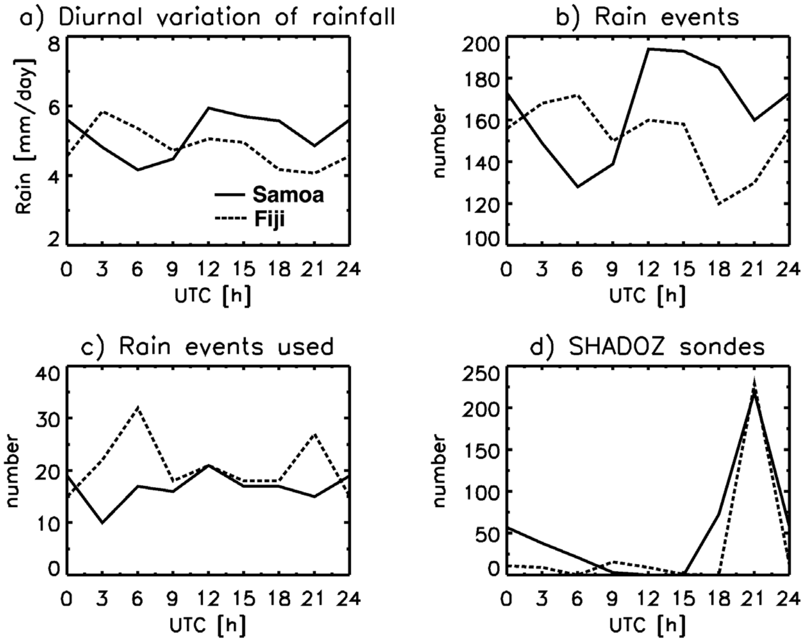

Figure 4. (a) Diurnal variation of the 2° × 2° TRMM rainfall at Samoa (solid line) and Fiji (dashed line), (b) total number of rain events per 3 h interval for a rainfall threshold of 1.5 mm/h, (c) number of rain events used to calculate the ozone anomaly patterns, and (d) diurnal variation in the launch time of the SHADOZ soundings. Local solar noon varies over the course of a year at Fiji between 23:50 and 00:20 UTC. Local solar noon at Samoa is between 23:10 and 23:40 UTC.

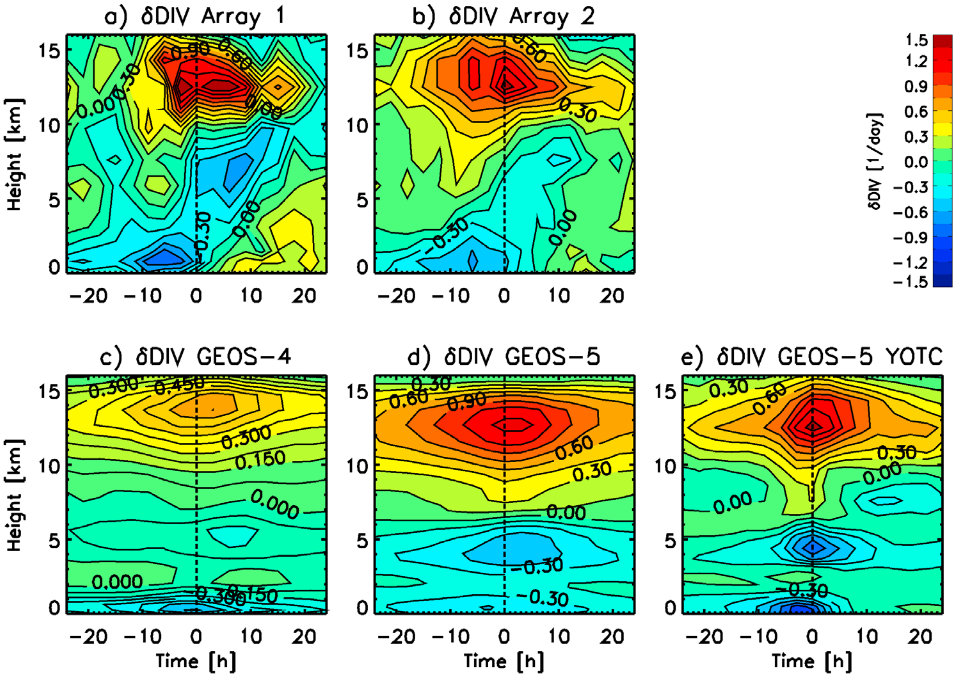

Figure 5. Divergence anomaly patterns about high rainfall events. The anomalies are with respect to seasonal mean profiles. The rain event threshold for the observed divergence anomaly patterns was 1.5 mm/h. For the models, we used a rain threshold of 1.0 mm/h. (a) Observed divergence anomaly pattern over array 1 and (b) observed divergence anomaly pattern over array 2 using IGRA radiosonde data. (c) Divergence anomaly generated using GEOS-4 meteorology, (d) divergence anomaly generated using GEOS-5 meteorology, and (e) divergence anomaly generated using a version of GEOS-5 with higher spatial resolution (Year of Tropical Convection, YOTC).

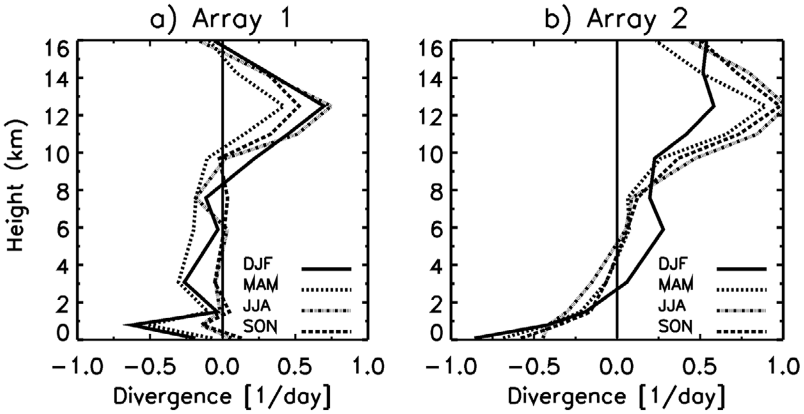

Figure 6. Seasonal mean divergence profiles of (a) array 1 and (b) array 2 from 1998 to 2009, averaged over all times in which the rain rate within each array exceeded 4 mm/d. The locations of arrays 1 and 2 are shown in Figure 1.

rainfall and a convergence 8 h after peak rainfall. The midlevel divergence maximum prior to peak rainfall has been interpreted as a signature of cumulus congestus clouds [*Thompson et al.*, 1979; *Mapes et al.*, 2006; *Mitovski et al.*, 2010]. The midlevel convergence maximum after peak rainfall can be attributed to precipitating stratiform anvil clouds. These clouds are associated with a downdraft mass flux that increases below the melting level (~5.5 km). The required downdraft entrainment can be expected to be balanced in part by an inward convergent mass flux from the background atmosphere.

[32] The midlevel divergence dipole of array 1 is stronger than the divergence dipole of array 2. This difference may be due to the difference in area between the two arrays. For a given average rain rate, a larger radiosonde array will in general contain a greater mixture of cloud types at different stages of development than a smaller array. In particular, one would expect a larger array to contain a more diverse mixture of congestus and precipitating stratiform anvil clouds. Because the congestus divergence and stratiform convergence features occur at the same height, and are of opposite sign, they tend to cancel in a spatial average. The midlevel divergence dipole can therefore be expected to become progressively weaker when defined for rain events of larger arrays [*Folkins et al.*, 2008]. The larger size of array 2 may therefore account for the weakness of its midlevel divergence dipole relative to array 1.

[33] The progressive disappearance of the midlevel divergence dipole, in response to an increase in size of the averaging region, also applies to temporal averages. Figure 6 shows the climatological divergence profiles of arrays 1 and 2 from 1998 to 2009, averaged over all times in which the rain rate within each array exceeded 4 mm/d. Although the deep outflow mode is very prominent, there is no evidence of a congestus divergence or a stratiform convergence. This demonstrates the importance of using divergence anomaly patterns about high rain events to isolate these features.

3.4. Mass Divergence Anomaly Patterns From GEOS-4 and GEOS-5

[34] Meteorological data sets can be used to construct mass divergence anomaly patterns about high rain events using a procedure similar to that described above for radiosonde arrays, except that the divergence is calculated from spatial derivatives in the horizontal wind using wind information at the four closest grid cells. As discussed previously, we also used a lower rain event threshold for the GEOS-4 and GEOS-5 rain events (1.0 mm/h rather than 1.5 mm/h), and considered rain events at two nearby grid cells in addition to the grid cells containing Fiji and Samoa.

[35] The mass divergence anomaly patterns of these four grid cells are shown in Figures 5c and 5d. The divergence anomaly patterns of GEOS-4 and GEOS-5 show some features that are consistent with observations. These include a boundary layer convergence feature and an upper tropospheric divergence feature. However, unlike the observations, the boundary layer convergence features of GEOS-4 and GEOS-5 are coincident rather than prior to peak rainfall. In addition, the GEOS-4 and GEOS-5 divergence anomaly patterns do not exhibit a midlevel divergence dipole. Instead, the two models exhibit a midlevel convergence maximum centered at peak rainfall (t = 0). These differences are consistent with previous results showing that the midlevel divergence dipole is poorly represented in both climate models and assimilated meteorological data sets [*Mitovski et al.*, 2010]. Figure 5 also shows that the GEOS-4 divergence anomalies are smaller than the GEOS-5 divergence anomalies. This is consistent with the smaller enhancement above background of the GEOS-4 rainfall rates during rain events (shown in Figure 3a).

[36] The weaknesses in the representation of the midlevel divergence dipole in global models could be due in part to a lack of spatial resolution. We have therefore calculated the mass divergence anomaly pattern of the higher spatial resolution (0.25° × 0.33°) YOTC version of GEOS-5. We looked for rain events at the 12 grid cells in this high-resolution data set nearest the two IGRA radiosonde arrays. These were located between 165°E and 180°E and 4°S and 4°N, and are indicated by circles in Figure 1. The rainfall frequency distribution of the 12 grid cells is shown in Figure 3b. Although there is a slightly increased incidence of high rainfall rates, it is similar to the rain frequency distribution of the lower spatial resolution version of GEOS-5 (shown in blue). High rain events from the high spatial resolution version of GEOS-5

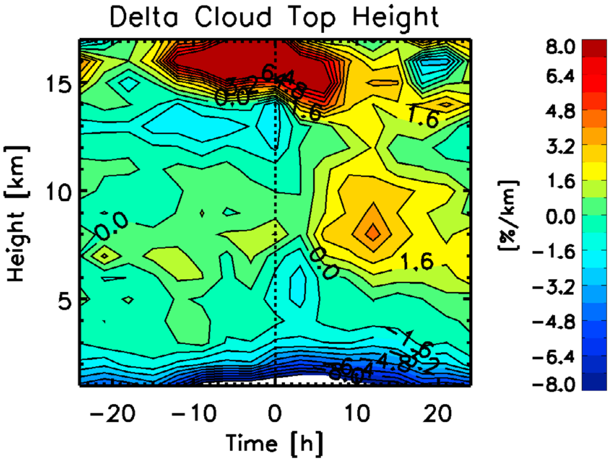

Figure 7. Cloud top frequency anomaly patterns. The anomaly pattern was generated using the 1 km horizontal resolution CALIPSO cloud top measurements and 2° × 2° TRMM 3B42 rainfall data over 15 tropical locations (shown with crosses in Figure 1) for the period between 2006 and 2009.

were therefore also considered to occur during times at which the rain rate exceeded 1.0 mm/h.

[37] Figure 5e shows the mass divergence anomaly pattern of the high-resolution GEOS-5 YOTC data set, evaluated at the 12 grid cells discussed above. It is similar to the divergence pattern produced by the lower spatial resolution version of GEOS-5. The main difference with the observed anomaly pattern is that the midlevel convergence feature occurs at t = 0, whereas the observed anomaly pattern exhibits a midlevel divergence dipole that is antisymmetric about t = 0.

[38] Although the intensity of a divergence anomaly patterns is sensitive to the rain event threshold, the overall shape of the anomaly pattern is not strongly sensitive to this threshold. It can be shown that the high-resolution divergence anomaly pattern generated using a rain event thresholds of 1.5 mm/h is similar to the pattern generated using a threshold of 1.0 mm/h.

3.5. Cloud Top Frequency Anomaly Pattern From CALIPSO

[39] Cloud top height measurements do not give direct insight into the vertical profile of mass detrainment from a convective cloud, except that one can usually assume that convective outflow is vertically distributed between cloud base and cloud top. Nevertheless, cloud top anomaly patterns about high rain events do provide an interesting complement to the mass divergence patterns discussed above.

[40] The cloud top anomaly patterns were produced as follows. We first looked for 2° × 2° TRMM rain events from the 2006–2009 CALIPSO period at the 15 locations indicated by crosses in Figure 1 (again using the 1.5 mm/h TRMM rain event threshold). Once a TRMM rain event was identified, we searched for 1 km horizontal resolution CALIPSO profiles (both cloudy and clear) inside the fifteen 2° × 2° grid cells that occurred within 24 h of a TRMM event. The vertical resolution of the cloud top data of each profile was reduced to 1 km, and each profile was assigned to a 3 h time bin on the basis of the difference between the CALIPSO measurement time and the time of the TRMM rain event. The number of cloud tops in each 1 km layer and 3 h time bin was then normalized by the total number of CALIPSO profiles (cloudy + clear sky) used in that time/height bin. This procedure was repeated for each season. Finally, we subtracted the seasonal mean cloud top frequency from the cloud top patterns for each season, and then averaged the four anomaly patterns together. This produced the annual mean cloud top frequency anomaly pattern shown in Figure 7.

[41] The most prominent feature of the cloud top frequency anomaly pattern is a very strong positive anomaly that develops at upper levels 12 h prior to peak rainfall (t = 0). The onset of this anomaly is roughly coincident with the onset of the deep convective divergence anomaly shown in Figures 5a and 5b. The 3 km vertical offset between the deep convective divergence (~13 km) and cloud top frequency (~16 km) anomalies demonstrates the absence of a direct relationship between mass outflow and cloud top height. The upper level cloud top anomaly is probably due to some combination of direct injection of ice crystals from deep convective detrainment, and in situ ice crystal formation that develops in response to an upper level cooling near 16 km that occurs in association with high rain events [*Mitovski et al.*, 2010].

[42] Figure 8 shows the seasonal mean cloud top frequency profiles from all 15 grid cells. The overall shape of this profile is consistent with cloud top frequency climatologies from previous lidar measurements [*Dessler et al.*, 2006]. The modest peak between 5 and 8 km of about 4% per km can be attributed to congestus clouds.

[43] The cloud top anomaly pattern shows that there is an absolute increase of 1–3% per km in the frequency of

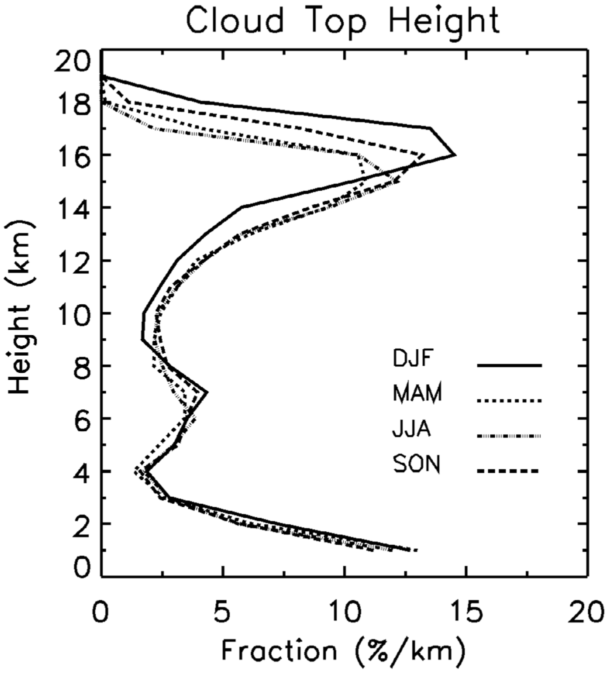

Figure 8. Seasonal mean cloud top frequency profiles from all 15 grid cells. The crosses in Figure 1 show the locations of the 15 grid cells. The profiles were calculated using CALIPSO measurements for the period 2006–2009.

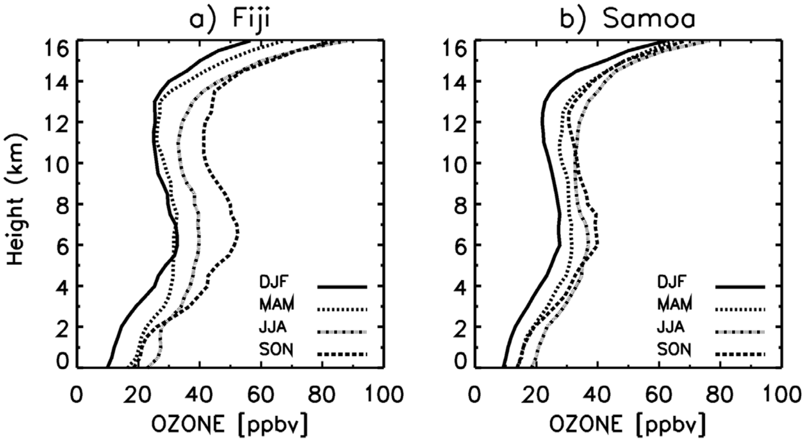

Figure 9. Seasonal mean ozone profiles at (a) Fiji and (b) Samoa. The seasonal profiles were calculated using SHADOZ soundings for the period 1998–2009.

occurrence of cloud tops between 5 and 8 km up to 15 h prior to peak rainfall (t = 0). This corresponds to a relative increase above background of about 50%. Some of the congestus clouds that develop prior to peak rainfall are probably obscured by the increased incidence of high-altitude cirrus clouds. As a result, the magnitude of the midlevel cloud top enhancement prior to peak rainfall may be underestimated.

[44] The cloud top anomaly pattern also shows that there is an increased incidence of clouds with tops between 5 and 12 km that develops after peak rainfall. This corresponds to a period when an increased incidence of stratiform anvil clouds is expected. This increase is coincident with a decrease in the occurrence of high-altitude cirrus clouds. Presumably, this decrease allows the lidar to penetrate to lower heights, and measure cloud tops that had previously been obscured.

[45] The cloud top anomaly pattern shown in Figure 7 was constructed using CALIPSO observations from both local noon and local midnight crossing times. Although there is a diurnal cycle in cloudiness associated with the diurnal cycle in rainfall over the oceans, it can be shown that the cloud top anomaly patterns produced by the two sets of profiles are similar.

4. Ozone

4.1. Ozone Anomaly Patterns From SHADOZ Observations

[46] Rapid rates of ozone destruction generate low ozone mixing ratios in the tropical marine boundary layer. Layers of preferred convective detrainment should therefore be associated with negative ozone anomalies. Figure 9 shows seasonal mean ozone mixing ratio profiles at Fiji and Samoa, generated by all SHADOZ measurements from 1998 to 2009. The upper tropospheric minimum in ozone mixing ratio near 13 km is characteristic of oceanic regions with frequent deep convection, and has been attributed to a local maximum in deep convective outflow at the same altitude [*Lawrence et al.*, 2003, *Folkins and Martin*, 2005].

[47] There is no evidence in Figure 9 of a midtropospheric minimum in mean ozone mixing ratios associated with enhanced detrainment from congestus clouds. Instead, there is a local maximum in ozone mixing ratio near 6 km. This maximum has been attributed to a change in the sign of the rate of chemical ozone production. Ozone is chemically produced in the upper troposphere at a rate of 1–2 ppbv/d [*Jacob et al.*, 1996]. After detraining from a deep convective cloud, the ozone mixing ratio of an air parcel will therefore initially increase as it sinks toward the surface. However, the rate of ozone destruction from the $O(^1D)$ + $H_2O \rightarrow 2OH$ reaction increases with the rise in ambient water vapor concentrations. At some point, usually in the midtroposphere, the net ozone production becomes negative and the ozone mixing ratio of an air parcel will decrease with continued sinking toward the surface (at least in unpolluted regions). This change in net chemical production has been used to explain the decrease in climatological ozone mixing ratio below 6 km [*Folkins and Martin*, 2005]. However, it is likely that the ozone decrease below 6 km is at least partially attributable to increased detrainment from congestus clouds, both by direct injection of lower ozone air from the boundary layer, and by providing a source of water vapor. In this section, we use ozone anomaly patterns about high rain events to demonstrate that direct injection of low ozone air from the boundary layer does indeed generate negative ozone anomalies in the midtroposphere, and therefore has an impact on mean ozone profiles.

[48] Ozone anomaly patterns about high rain events were defined using a procedure similar to the procedure used above for the mass divergence and cloud top frequency anomaly patterns. We used all ozonesondes at Fiji and Samoa within 24 h of a TRMM rain event at the 2° × 2° grid cells containing Fiji and Samoa. The ozonesondes were grouped into 3 h time bins on the basis of the difference between the time of the ozonesonde launch and the time of the rainfall event. Ozone anomalies were calculated by taking the deviation from the appropriate seasonal mean, and then averaged to produce an annual mean ozone anomaly pattern. The ozone anomaly patterns at Fiji and Samoa were similar, and therefore combined into a single composite anomaly pattern. This composite pattern is shown in Figure 10a.

[49] The ozone anomaly pattern shows that negative ozone anomalies develop at midlevels roughly 16 h prior to peak

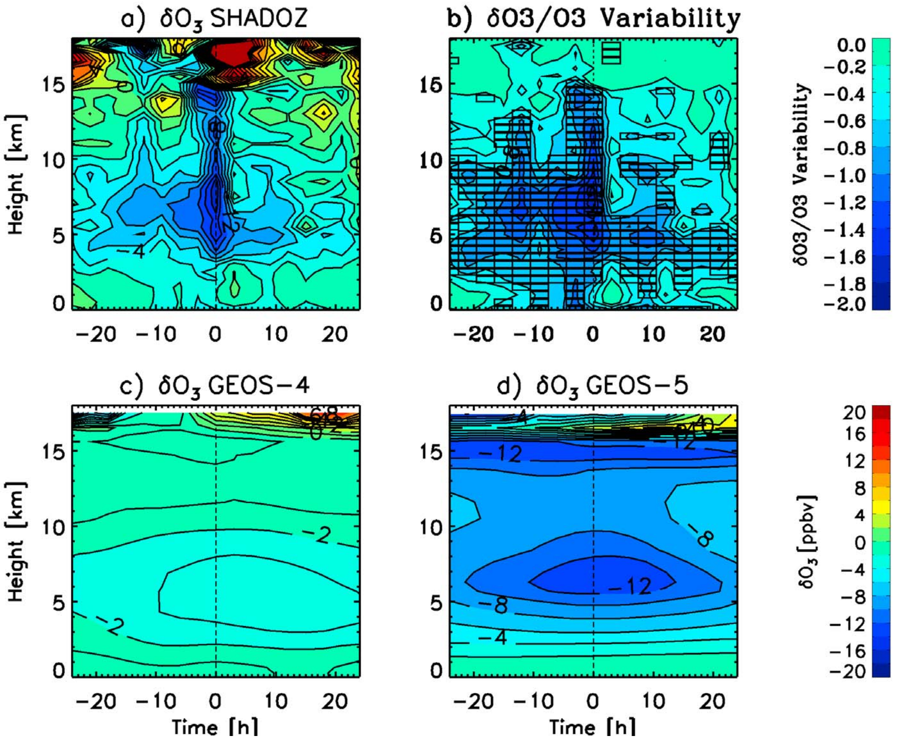

Figure 10. Observed and modeled ozone anomaly pattern about high rain events. The anomalies are with respect to seasonal mean profiles. The rain event threshold for the observed ozone anomaly patterns was 1.5 mm/h. For the models, we used a rain threshold of 1.0 mm/h. (a) Observed ozone anomalies at Fiji and Samoa using SHADOZ data. (b) Ratio of the ozone anomalies in Figure 10a to the background variability. The black rectangles show the locations of the mean ozone anomalies that are considered to be significant according to a version of *t* test with $p = 0.05$. (c) Ozone anomalies from GEOS-Chem using GEOS-4 meteorology, and (d) ozone anomalies from GEOS-Chem using GEOS-5 meteorology.

rainfall. This midlevel ozone decrease develops in concert with enhancements in the frequency of midlevel cloud tops, and extends over a similar altitude range (4–8 km). The midlevel negative ozone anomalies that develop prior to peak rainfall can therefore be attributed to increased detrainment from congestus clouds.

[50] Within several hours of peak rainfall ($t = 0$), there is a strong negative ozone anomaly that extends from the boundary layer to the tropopause. The duration of this full depth negative ozone anomaly is approximately coincident with the upper level divergence anomaly, and can therefore be attributed to enhanced outflow from deep convection.

[51] Figure 10a also shows that positive ozone anomalies develop near the tropopause (∼17 km) after peak rainfall. These ozone anomalies appear to be associated with the propagation of Kelvin waves.

4.2. Ozone Anomaly Patterns From GEOS-Chem

[52] Rain events were selected from the GEOS-4 and GEOS-5 precipitation data sets using the same procedure previously used when constructing the GEOS-4 and GEOS-5 divergence anomaly patterns. We then selected ozone profiles from the GEOS-Chem model within 24 h of the GEOS-4 and GEOS-5 rain events between January 2004 and December 2006. Ozone anomalies were calculated by taking the difference from seasonal mean ozone profiles defined over the same time period. The ozone anomaly patterns generated by the GEOS-Chem model using GEOS-4 and GEOS-5 meteorology are shown in Figures 10c and 10d. The GEOS-4 ozone anomalies are about twice as small as the GEOS-5 ozone anomalies. This is consistent with the relative strength of the GEOS-4 and GEOS-5 divergence anomalies, and appears to reflect the smaller increase above background of the GEOS-4 rain rates during rain events.

[53] In both GEOS-4 and GEOS-5, convection gives rise to two layers of reduced ozone, roughly centered at 6 and 16 km. The midlevel ozone reductions of the two GEOS-Chem simulations are roughly symmetric about peak rainfall ($t = 0$), whereas the observed midlevel ozone reductions are strongest prior to peak rainfall. Both versions of GEOS-Chem exhibit upper level negative ozone anomalies that are much more persistent than the observations, presumably reflecting the greater persistence of the GEOS-4 and GEOS-5 rain events (shown in Figure 3a).

4.3. Statistical Significance of Observed Ozone Anomalies

[54] The ozone anomaly pattern shown in Figure 10a is clearly noisy, and some of the features would probably not appear in an anomaly pattern constructed from a larger

number of ozonesondes. One way to assess the statistical significance of the ozone anomaly $\overline{\delta O_3}(z,t)$ of a given height-time bin is to divide the anomaly by a measure of the variability in background ozone. We calculated the vertical profile of the standard deviation in ozone mixing ratio at Fiji and Samoa for each of the four seasons using the following formula:

$$\sigma_{all}(z) = \sqrt{\frac{1}{m-1}\sum_{i=1}^{m}\left[O_{3,i}(z) - \overline{O_3}(z)\right]^2}. \qquad (1)$$

$O_{3,i}(z)$ refers to an ozone measurement at height z from sonde i; m refers to the total number of sondes at Fiji or Samoa between 1998 and 2009 during a season, and $\overline{O_3}(z)$ refers to the appropriate seasonal climatological profile. The four seasonal standard deviation profiles of each location were averaged to produce a combined annual mean standard deviation for Fiji and Samoa. The ratio of the mean ozone anomaly to the standard deviation is shown in Figure 10b. In general, the ozone anomaly exceeds the background variability in regions where the anomaly itself is largest: at midlevels prior to peak rainfall, and throughout the troposphere during high rainfall events.

[55] We also used a version of the t test to determine the statistical significance of the ozone anomalies. In this test, the mean ozone anomaly of each bin is divided by a standard deviation that is calculated from the ozone anomalies of the rain events.

$$T_{test} = \frac{\overline{\delta O_3}(z,t)}{\sqrt{\sigma_{event}{}^2(z,t)/n}}. \qquad (2)$$

[56] The standard deviation of the event ozone anomalies is give by

$$\sigma_{event}(z,t) = \sqrt{\frac{1}{n-1}\sum_{i=1}^{n}\left[\delta O_{3,i}(z,t) - \overline{\delta O_3}(z,t)\right]^2}, \qquad (3)$$

where $\delta O_{3,i}(z,t)$ refers to a rain event ozone anomaly at height z from sonde i, and n is the total number of ozone anomaly measurements in a particular time/height bin (typically around 20). The mean ozone anomalies are considered to be significant if the value of T_{test} is greater than a particular tabulated value $T_{crit}(n,p)$ [*Armitage et al.*, 2002], where p refers to the likelihood that the observed mean anomalies could have been generated by chance alone. Here, we used 95% statistical significance threshold, setting $p = 0.05$. The black rectangles in Figure 10b show the locations of the mean ozone anomalies that are considered significant according to this criterion.

[57] Some features of the observed ozone anomaly pattern are unlikely to be robust, despite being considered statistically significant according to the t test. For example, the mean TRMM rain event profile shown in Figure 3a was constructed from only those rain events at Fiji and Samoa between 1998 and 2009 that occurred within 24 h of an ozonesonde. It exhibits a secondary rainfall peak at -12 h that appears to be associated with coincident negative ozone anomalies above 8 km. However, this secondary rainfall peak does not appear in the mean TRMM rain event profile constructed from all rain events at Fiji and Samoa between 1998 and 2009. It is therefore unlikely that the negative ozone anomaly above 8 km at -12 h would occur in an ozone anomaly pattern constructed from an ozonesonde data set with a higher sampling rate (i.e., more frequent than the biweekly sampling rate used in SHADOZ).

5. Lightning

[58] We have attributed the negative ozone anomalies associated with high rain events to the effects of convective transport. However, lightning also occurs during deep convection and affects the ozone budget in a variety of ways. The NO that is produced by lightning destroys ozone on short time scales (due to the reaction of NO with ozone), but produces ozone on longer time scales. In situ measurements of lightning NO_x ($NO + NO_2$) in the vicinity of deep convection were made during the Stratospheric Climate Links with Emphasis on the Upper Troposphere and Lower Stratosphere (SCOUT-O3) and Aerosol and Chemical Transport in Deep Convection (ACTIVE) aircraft campaigns, conducted over northern Australia in November–December 2005 [*Vaughan et al.*, 2008]. NO_x enhancements due to lightning were about 1 ppbv in the upper troposphere, and less than 0.5 ppbv in the middle troposphere [*Huntrieser et al.*, 2009]. In the tropics, lightning is much less frequent over the oceans than over land [*Christian et al.*, 2003], so these NO_x enhancements should be considered an upper limit for Fiji and Samoa. On the short time scales relevant to this analysis, the expected decreases in ozone associated with lightning generated NO can be assumed to be less than 1 ppbv.

6. Summary

[59] This paper has outlined a new methodology for assessing the impact of convection on the background distribution of a chemical tracer. Rain events in the western equatorial Pacific were identified using particular thresholds for spatial extent, intensity, and duration. The spatial extent threshold is intended to ensure that the rain events are synoptic in scale rather than being associated with mesoscale diurnally forced circulations.

[60] Once rainfall events were identified, we constructed anomaly patterns in the time height plane that help characterize the imprint of convection on the background fields of mass divergence, cloud top height frequency, and ozone mixing ratio. There has recently been increased recognition of the importance of the layered character of tropical convective outflow [*Thompson et al.*, 1979; *Johnson et al.*, 1999]. The impact of the deep outflow mode can be immediately identified in climatological profiles of divergence, cloud top frequency, and ozone. The impact of the congestus outflow mode on the climatological profiles of divergence and ozone mixing ratio is much less apparent. The effects of the congestus outflow mode on the background distributions of mass and ozone can only be determined through the use of anomaly patterns about high rain events. We have found that the onset of midlevel (3–8 km) negative ozone anomalies occurs approximately 16 h prior to peak rainfall. Modest increases in midlevel cloud top frequency occur over a similar time period, and support the interpretation that the negative midlevel ozone

anomalies prior to peak rainfall can be attributed to enhanced detrainment from congestus clouds. The divergence field exhibits a delayed response to the increased frequency of congestus clouds, with a local maximum in midlevel divergence appearing about 8 h prior to peak rainfall.

[61] In global chemical transport models, the spatial scale of convective clouds is much smaller than the grid scale, so that the convective transport of chemical tracers is parameterized rather than explicitly modeled. The observationally based divergence and ozone anomaly patterns discussed here should provide useful diagnostics for testing the accuracy of this parameterized vertical transport. In agreement with a previous comparison [*Mitovski et al.*, 2010], we found the midlevel divergence dipole is poorly represented in two assimilated meteorological data sets. In particular, the two models had difficulty representing the midlevel temporal asymmetry in the divergence field associated with congestus divergence prior to peak rainfall, and stratiform convergence after peak rainfall.

[62] The ozone anomaly patterns of the GEOS-Chem chemical transport model, when forced by GEOS-4 and GEOS-5 assimilated meteorology, exhibit both midlevel and upper tropospheric negative ozone anomalies. However, the upper tropospheric negative ozone anomalies of the two simulations are much more persistent than in the observations. This difference is probably due to the excessive persistence of the GEOS-4 and GEOS-5 rain events. At midlevels, the negative ozone anomalies of the GEOS-Chem simulations are roughly symmetric about peak rainfall ($t = 0$), whereas the observed midlevel ozone anomalies are strongest prior to peak rainfall. This lack of asymmetry in the midlevel ozone response of the two models is probably due to the lack of asymmetry in the midlevel divergence anomalies of the GEOS-4 and GEOS-5 assimilated meteorological data sets.

[63] **Acknowledgments.** The authors acknowledge useful discussions with Kenneth Pickering, Mark Lawrence, and Jeffrey Pierce. We thank the following institutions for making their data public: NASA GSFC (TRMM 3B42 and SHADOZ), NCDC (IGRA), NASA GMAO (GEOS-4 and GEOS-5), and NASA LARC (CALIPSO). Comments and suggestions by three anonymous reviewers greatly improved the manuscript. This research was supported by the Natural Sciences and Engineering Research Council (NSERC) of Canada.

References

Armitage, P., G. Berry, and J. N. S. Matthews (2002), *Statistical Methods in Medical Research*, 4th ed., Blackwell Sci., Oxford, U. K., doi:10.1002/9780470773666.

Avery, M., et al. (2010), Convective distribution of tropospheric ozone and tracers in the Central American ITCZ region: Evidence from observations during TC4, *J. Geophys. Res.*, *115*, D00J21, doi:10.1029/2009JD013450.

Bey, I., et al. (2001), Global modeling of tropospheric chemistry with assimilated meteorology: Model description and evaluation, *J. Geophys. Res.*, *106*, 23,073–23,095, doi:10.1029/2001JD000807.

Christian, H. J., et al. (2003), Global frequency and distribution of lightning as observed from space by the Optical Transient Detector, *J. Geophys. Res.*, *108*(D1), 4005, doi:10.1029/2002JD002347.

Dessler, A. E., S. P. Palm, and J. D. Spinhirne (2006), Tropical cloud-top height distributions revealed by the Ice, Cloud, and Land Elevation Satellite (ICESat)/Geoscience Laser Altimeter System (GLAS), *J. Geophys. Res.*, *111*, D12215, doi:10.1029/2005JD006705.

Durre, I., R. S. Vose, and D. B. Wuertz (2006), Overview of the Integrated Global Radiosonde Archive, *J. Clim.*, *19*(1), 53–68, doi:10.1175/JCLI3594.1.

Folkins, I., and R. V. Martin (2005), The vertical structure of tropical convection and its impact on the budgets of water vapor and ozone, *J. Atmos. Sci.*, *62*, 1560–1573, doi:10.1175/JAS3407.1.

Folkins, I., C. Braun, A. M. Thompson, and J. C. Witte (2002), Tropical ozone as an indicator of deep convection, *J. Geophys. Res.*, *107*(D13), 4184, doi:10.1029/2001JD001178.

Folkins, I., et al. (2006), Testing convective parameterizations with tropical measurements of HNO_3, CO, H_2O, and O_3: Implications for the water vapor budget, *J. Geophys. Res.*, *111*, D23304, doi:10.1029/2006JD007325.

Folkins, I., S. Fueglistaler, G. Lesins, and T. Mitovski (2008), A low-level circulation in the tropics, *J. Atmos. Sci.*, *65*, 1019–1034, doi:10.1175/2007JAS2463.1.

Hack, J. J. (1994), Parameterization of moist convection in the National Center for Atmospheric Research Community Climate Model (CCM2), *J. Geophys. Res.*, *99*, 5551–5568, doi:10.1029/93JD03478.

Huntrieser, H., et al. (2009), NO_x production by lightning in Hector: First airborne measurements during SCOUT-O_3/ACTIVE, *Atmos. Chem. Phys.*, *9*, 8377–8412, doi:10.5194/acp-9-8377-2009.

Jacob, D. J., et al. (1996), Origin of ozone and NO_x in the tropical troposphere: A photochemical analysis of aircraft observations over the South Atlantic basin, *J. Geophys. Res.*, *101*, 24,235–24,250, doi:10.1029/96JD00336.

Johnson, R. H., et al. (1999), Trimodal characteristics of tropical convection, *J. Clim.*, *12*, 2397–2418, doi:10.1175/1520-0442(1999)012<2397:TCOTC>2.0.CO;2.

Kley, D., et al. (1996), Observations of near-zero ozone concentrations over the convective Pacific: Effects on air chemistry, *Science*, *274*, 230–233, doi:10.1126/science.274.5285.230.

Kummerow, C., et al. (1998), The Tropical Rainfall Measuring Mission (TRMM) Sensor Package, *J. Atmos. Oceanic Technol.*, *15*(3), 809–817, doi:10.1175/1520-0426(1998)015<0809:TTRMMT>2.0.CO;2.

Lawrence, M. G., P. J. Crutzen, and P. J. Rasch (1999), Analysis of the CEPEX ozone data using a 3D chemistry-meteorology model, *Q. J. R. Meteorol. Soc.*, *125*, 2987–3009, doi:10.1256/smsqj.56009.

Lawrence, M. G., R. von Kuhlmann, M. Salzmann, and P. J. Rasch (2003), The balance of effects of deep convective mixing on tropospheric ozone, *Geophys. Res. Lett.*, *30*(18), 1940, doi:10.1029/2003GL017644.

Lelieveld, J., and P. J. Crutzen (1994), Role of deep cloud convection in the ozone budget of the troposphere, *Science*, *264*, 1759–1761, doi:10.1126/science.264.5166.1759.

Liu, J., J. A. Logan, D. B. A. Jones, N. J. Livesey, I. A. Megretsakaia, C. Cargouge, and P. Nedelec (2010), Analysis of CO in the tropical troposphere using Aura satellite data and the GEOS-Chem model: Insights into transport characteristics of the GEOS meteorological products, *Atmos. Chem. Phys.*, *10*, 12,207–12,232, doi:10.5194/acp-10-12207-2010.

Mapes, B. E., S. Tulich, J. Lin, and P. Zuidema (2006), The mesoscale convection life cycle: Building block or prototype for large-scale tropical waves?, *Dyn. Atmos. Oceans*, *42*, 3–29, doi:10.1016/j.dynatmoce.2006.03.003.

Mitovski, T., I. Folkins, K. von Salzen, and M. Sigmond (2010), Temperature, relative humidity, and divergence response to high rainfall events in the tropics: Observations and models, *J. Clim.*, *23*, 3613–3625, doi:10.1175/2010JCLI3436.1.

Moorthi, S., and M. J. Suarez (1992), Relaxed Arakawa-Schubert: A parameterization of moist convection for general-circulation models, *Mon. Weather Rev.*, *120*, 978–1002, doi:10.1175/1520-0493(1992)120<0978:RASAPO>2.0.CO;2.

Nassar, R., J. A. Logan, I. A. Megretskaia, L. T. Murray, L. Zhang, and D. B. A. Jones (2009), Analysis of tropical tropospheric ozone, carbon monoxide, and water vapor during the 2006 El Niño using TES observations and the GEOS-Chem model, *J. Geophys. Res.*, *114*, D17304, doi:10.1029/2009JD011760.

Nesbitt, S. W., and E. J. Zipser (2003), The diurnal cycle of rainfall and convective intensity according to three years of TRMM measurements, *J. Clim.*, *16*, 1456–1475, doi:10.1175/1520-0442-16.10.1456.

Pickering, K. E., A. M. Thompson, W.-K. Tao, and T. L. Kucsera (1993), Upper tropospheric ozone production following mesoscale convection during STEP/EMEX, *J. Geophys. Res.*, *98*, 8737–8749, doi:10.1029/93JD00875.

Pickering, K. E., et al. (2001), Trace gas transport and scavenging in PEM-Tropics B South Pacific Convergence Zone convection, *J. Geophys. Res.*, *106*, 32,591–32,602, doi:10.1029/2001JD000328.

Solomon, S., et al. (2005), On the distribution and variability of ozone in the tropical upper troposphere: Implications for tropical deep convection and chemical-dynamical coupling, *Geophys. Res. Lett.*, *32*, L23813, doi:10.1029/2005GL024323.

Thompson, A. M., et al. (2003), Southern Hemisphere Additional Ozonesondes (SHADOZ) 1998–2000 tropical ozone climatology: 1. Comparison with Total Ozone Mapping Spectrometer (TOMS) and ground-based measurements, *J. Geophys. Res.*, *108*(D2), 8238, doi:10.1029/2001JD000967.

Thompson, R. M., Jr., S. W. Payne, E. E. Recker, and R. J. Reed (1979), Structure and properties of synoptic-scale wave disturbances in the Intertropical Convergence Zone of the eastern Atlantic, *J. Atmos. Sci.*, *36*, 53–72, doi:10.1175/1520-0469(1979)036<0053:SAPOSS>2.0.CO;2.

Vaughan, G., et al. (2008), SCOUT-O_3/ACTIVE high-altitude aircraft measurements around deep tropical convection, *Bull. Am. Meteorol. Soc.*, *89*, 647–662, doi:10.1175/BAMS-89-5-647.

Winker, D. M., M. A. Vaughan, A. Omar, Y. Hu, K. A. Powell, Z. Liu, W. H. Hunt, and S. A. Young (2009), Overview of the CALIPSO mission and CALIOP data processing algorithms, *J. Atmos. Oceanic Technol.*, *26*, 2310–2323, doi:10.1175/2009JTECHA1281.1.

Zhang, G. J., and N. A. McFarlane (1995), Sensitivity of climate simulations to the parameterization of cumulus convection in the CCC-GCM, *Atmos. Ocean*, *33*, 407–446, doi:10.1080/07055900.1995.9649539.

Zuidema, P. (1998), The 600–800 mb minimum in tropical cloudiness observed during TOGA COARE, *J. Atmos. Sci.*, *55*, 2220–2228, doi:10.1175/1520-0469(1998)055<2220:TMMITC>2.0.CO;2.

M. Cooper, I. Folkins, R. V. Martin, and T. Mitovski, Department of Physics and Atmospheric Science, Dalhousie University, Halifax, NS B3H 4R2, Canada. (mitovski@dal.ca)